Article

Utilization of Low-Rank Coal and Zn-Bearing Dusts for Preparation of K, Na-Embedded Porous Carbon Material and Metallized Pellets by Synergistic Activation and Reduction Process

Dingzheng Wang [1], Deqing Zhu [2,*], Jinlin Yang [1,*] and Shaojian Ma [1]

[1] State Key Laboratory of Featured Metal Materials and Life-Cycle Safety for Composite Structures, MOE Key Laboratory of New Processing Technology for Nonferrous Metals and Materials, School of Resources, Environment and Materials, Guangxi University, Nanning 530004, China; dingzheng_wang@163.com (D.W.); msj@gxu.edu.cn (S.M.)

[2] School of Minerals Processing and Bioengineering, Central South University, Changsha 410083, China

* Correspondence: dqzhu@csu.edu.cn (D.Z.); jlyang523@126.com (J.Y.)

Abstract: A technology was developed for managing Zn-bearing dust, facilitating the recycling of hazardous solid waste and the production of porous carbon materials. In the one-step process, Zn-bearing dusts were employed not only as raw materials to prepare reduced Zn-bearing dust pellets but also as activators to prepare K, Na-embedded activated carbon. In the process, the Fe, C, Zn, K, and Na in the dusts were rationally utilized. Under optimal conditions, the reduced pellets and porous carbon materials were simultaneously produced and characterized using XRD, SEM/EDS, FTIR, and adsorption of nitrogen techniques. The results indicated that the reduced pellets, with low levels of harmful elements and high iron grade and strength, could be directly used as burden for enhancing blast furnace operation without additional agglomeration. Meanwhile, the K and Na-embedded porous carbon material demonstrated superior SO_2 and NO adsorption capacities compared to the commercial activated carbon, making it suitable for purifying SO_2 and NO-bearing flue gas. The hazardous solid wastes were effectively used to treat flue gases through this technology. The mechanism in the synergistic reduction and activation process was elucidated. The coupling effect between the reduction reactions of Fe_2O_3, Fe_3O_4, FeO, $MgFe_2O_4$, $CaFe_2O_4$, $ZnFe_2O_4$, $KFeO_2$, and $NaFeO_2$ in the dusts and activation reaction of C in the coal promoted the synchronous reduction and activation process.

Keywords: Zn-bearing dusts; low-rank coal; porous carbon; reduction; activation; waste disposal

1. Introduction

Zn-bearing dusts (ZD) are primarily collected in the dedusting systems of blast furnace, converter and electric furnace [1–3], and account for 3–4% of crude steel output, and reached about 56–75 million tons in the world in 2023 [4]. The ZD are classified as environmentally hazardous wastes due to their relatively high concentrations of heavy metals (Pb and Zn), which can cause significant environmental pollution without proper management. In the meantime, it is difficult to directly recycle the dusts without removal of Zn from the dusts. The direct reduction technology, due to its high efficiency in removing hazardous metals such as K, Na, Zn, and Pb, has been extensively applied for processing dusts using rotary kiln and rotary hearth furnace methods [5,6]. The carbon-bearing pellets (CBP) made from the dusts are reduced at temperatures ranging from 1100 to 1300 °C during the direct reduction process. The hazardous metal oxides in the dusts can be reduced to their gaseous forms and volatilized into the flue gas, while the iron remains in the pre-reduced pellets. Subsequently, the zinc can be recovered from the flue gas, and the iron-rich pellets can be

directly recycled for ironmaking. In direct reduction, the removal efficiency of zinc and lead can exceed 90%, while potassium and sodium can be removed by up to 80% [7–9].

Currently, the problems, including the reduction degradation and zinc removal of Zn-bearing dust pellets (ZDP) with high energy consumption in the direct reduction process, constrain its application [10]. When pellets are reduced at high temperatures, the lattice transformation of hematite can cause the pellets to expand in volume, leading to increased fines production, resulting in accretion inside the rotary hearth furnace or rotary kiln and lowering the efficiency of the processes [11,12]. Additionally, using pre-reduced pellets with low compressive strength as charge in the blast furnace necessitates the implementation of certain measures, potentially leading to increased production costs. The reduction temperature for the zinc-bearing dusts is much higher than that of ordinary iron ores for the purpose of hazardous metals removal, which will lead to high energy consumption and poor economic performance [13]. Therefore, it is crucial to develop an effective solution to address these issues. In the coal-based direct reduction process of ZD, metal oxides were reduced by CO and produced CO_2, which serves as a typical activator for the preparation of activated carbon [14,15]. Moreover, the CO generated during the carbon activation process will promote the reduction of metal oxides in return. Theoretically, it seems that the chain reactions between the reduction of metal oxides in ZD and activation of carbon in the coal can realize the integration of direct reduction of ZD and preparation of coal-based activated carbon. Meanwhile, a catalytic effect on the activation of carbon is likely to be exerted by the zinc, potassium, and sodium in the dusts to some extent [16–18]. In previous studies, the zinc-bearing dusts were used as raw material for ironmaking after the removal of zinc [4]. In this study, the zinc-bearing dusts were not only used as raw material for preparation of blast furnace burden but also employed as an activator for the preparation of porous carbon material. Coal is widely used as a precursor for the production of coal-based commercial activated carbon due to its lower cost compared with other precursors, including resin, pitch, shell, and wood. The preparation process of coal-based activated carbon mainly comprises carbonization and activation. Usually, the reaction time of carbonization and activation processes of coal can reach up to 3 h, which will lead to low production efficiency and high energy consumption [19]. Therefore, developing a technology that integrates the carbonization and activation processes is of significant value.

An innovative process combining the direct reduction of metal oxides with the activation of carbon is proposed in this paper to address some limitations of traditional direct reduction methods. ZD from steel plants were made into CBP and utilized for preparation of metallized pellets and porous carbon material simultaneously. The high-value porous carbon material can significantly elevate the economic benefit of the process, while the high-strength reduced pellets can be used directly as a burden to improve blast furnace operations without the need for further agglomeration. In addition, the porous carbon material, which was prepared through a one-step activation process, can be utilized for flue gas desulfurization and denitrification. The adsorption capacity of the porous carbon material for acid gases (SO_2 and NO) was improved by the presence of alkali metal oxides (K_2O and Na_2O) in the material. In this study, the carbonization and activation of coal took place simultaneously in the high-temperature process, shorting the preparation time and elevating the production efficiency compared with the traditional preparation process of coal-based activated carbon. The carbon in the coal functioned as a reducing agent for ZD, whereas the dusts acted as activators for the carbon activation process. The coupling effect between the reduction of ZD and the activation of coal was elucidated. The activation process of the low-rank coal and the phases transformation and microstructure evolution of the ZDP in the process of synergistic activation and reduction were investigated.

2. Materials and Methods

2.1. Material

In this work, the raw materials collected from an iron and steel plant in Guangdong Province in China were as follows: two kinds of soft coal (SC and YC), one bentonite, and

three kinds of ZD, including the dust from converter (DAC), dust from blast furnace (DAB), and environmental dedusting dust of converter (DEC).

Image The ZD acted as activators for producing the porous carbons (PCs). The main chemical compositions of the ZD are listed in Table 1. It can be observed that the DAC was rich in Fe (56.09%), while the iron content in DAB and DEC was lower than 25%. The carbon-rich DAB could provide a reducing substance for the reduction of metal oxides in ZD. Besides zinc, relatively high contents of potassium (1.25%) and sodium (0.5%) in the blend may constrain the utilization of reduced ZD for ironmaking in a blast furnace [20]. Therefore, the removal rate of potassium and sodium was also investigated in this paper.

Table 1. Main chemical compositions of ZD (wt%).

Item	Fe_{total}	FeO	MFe	Zn	K	Na
DAC	56.09	26.55	1.72	3.15	0.25	0.18
DAB	24.07	13.30	0.69	7.82	3.13	0.96
DEC	19.81	14.87	0.09	1.38	1.29	1.56
Blend	44.07	21.71	1.2	4.63	1.25	0.50
C	**SiO_2**	**Al_2O_3**	**CaO**	**MgO**	**LOI^a**	**Adding ratio**
-	1.55	0.25	6.24	1.87	3.05	63
20.43	10.00	1.10	4.83	1.48	24.44	33
-	6.17	3.58	23.82	5.55	16.60	4
6.74	4.53	0.67	6.47	1.90	10.65	100

LOI^a—loss on ignition.

Image Usually, the agglomeration process is needed before the reduced ZD are used for ironmaking. In order to shorten the ironmaking process and improve reduction reactions in ZD, the three kinds of ZD were blended with reductant YC and made into carbon-containing pellets with bentonite as the binder. Bentonite contains 89% montmorillonite and can hold the particles of ZD together and provide cohesion in the green balls [21]. The percentage of particles less than 0.074 mm in the dusts and YC was both higher than 87 wt%, indicating that the size distribution of the materials was suited for pelletizing. Table 2 provides the proximate analysis of YC and the primary chemical compositions of its ash. It was observed that the Vad of YM reached up to 58.2%, which could lead to high porosity of the CBP and promote the diffusion of gases (CO, CO_2, K, Na, and Zn) in the pellets at high temperature. The SC with a diameter of 10~15 mm was used as a precursor of porous carbons. In the meantime, the SC could provide CO for reduction reactions in the ZDP. The proximate analysis of SC and main chemical compositions of its ash are shown in Table 2. Although the low-rank coal is abundant and cheap, it is classified as a non-renewable fossil fuel. Compared to coal, biomass is cleaner and renewable. Therefore, coal will be replaced by biomass in our further investigation.

Table 2. The proximate analysis of coals and chemical compositions of their ash (wt%).

Coal Types	Proximate Analysis				Main Chemical Compositions of Ash				
	M_{ad}	FC_{ad}	V_{ad}	A_{ad}	Fe_{total}	CaO	Al_2O_3	SiO_2	MgO
YC	5.6	31.4	58.2	4.7	4.5	28.2	20.7	19.5	21.9
SC	0.1	51.4	29.4	6.1	11.8	25.0	8.0	27.6	16.3

M_{ad}: Moisture, FC_{ad}: fixed carbon, V_{ad}: volatile matter, A_{ad}: ash.

2.2. Methods

Image This paper primarily investigates the preparation of reduced pellets from ZD and porous carbon materials, the characterization of these reduced pellets and porous carbons, and the demonstration of the mechanism underlying the synergistic reduction of metal oxides and activation of carbon. Figure 1 outlines the process for preparing the porous carbons and reduced pellets. Firstly, carbon-bearing green balls were prepared from a blend

of three types of ZD, reductant YC, and bentonite using a disc pelletizer. The mass ratio of YC and swell soil to the blend of ZD were set at 22% and 1%, respectively. Then, the green balls with diameters of 16~18 mm were dried in a vacuum drying oven at 105 °C for 2 h to produce dry pellets. Finally, the dry pellets were reduced, and the SC was activated in a shaft furnace. The experiment conditions were optimized in previous studies.
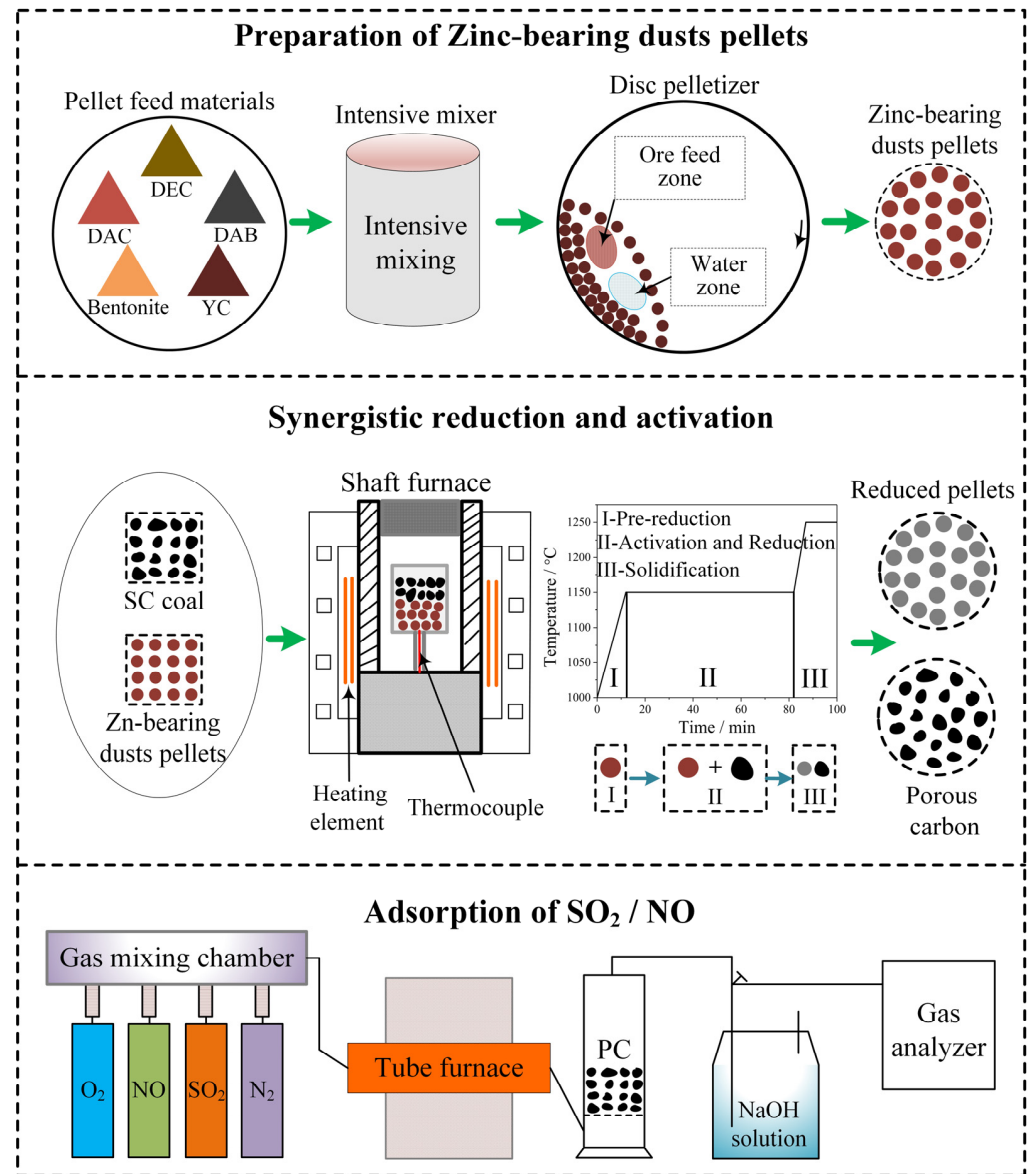
Figure 1. Schematic diagram of the preparation process of metallized pellets and PCs and characterization of SO_2/NO adsorption capacities of PCs.

When the furnace temperature reached 1000 °C, approximately 100 g of dry pellets was introduced into the preheated crucible. The furnace was heated at a rate of 12.5 °C/min, and the pellets underwent a non-isothermal pre-reduction process before the temperature was increased to 1150 °C. Then, some coarse SC was added into the crucible to cover the pellets, and the synergistic reduction of metal oxides and carbonization and activation of carbon began to proceed. The C/O molar ratio, defined as the ratio of fixed carbon in the SC and dry pellets to reducible oxygen in the dry pellets, was set at 1.25 and 2.5. After 70 min of isothermal reaction at 1150 °C, the temperature was raised to 1250 °C in 7 min and then kept for 13 min at this temperature for solidification of the reduced pellets. Finally,

the reduced pellets and porous carbon materials were cooled down under the protection of N_2 and separated through dry magnetic separation.

The adsorption capacities of the porous carbon for SO_2 and NO were evaluated separately through the apparatus, which is shown in Figure 1. The composition of the mixed gas was set according to the sintering flue gas in BAO steel of China. The inlet gas was adjusted to have an O_2 volume concentration of 12%, while the mixed gas contained SO_2 and NO at concentrations of 1800 mg/m^3 and 360 mg/m^3, respectively. The mixed gas with a temperature of 80 °C flowed through the porous carbons with a space velocity of 2100 h^{-1}. A flue gas analyzer (MGA 5, MRU, Berlin, Germany) was used to monitor and record the concentrations of SO_2 and NO. The experiment was terminated when the removal efficiency of SO_2/NO dropped below 20%. The SO_2/NO adsorption capacity (mg/g) of the porous carbons was calculated by integrating the areas under the adsorption curves along with considering the space velocity and the gas concentration of the mixed gas before adsorption.

The low-temperature N_2 adsorption–desorption isotherms were determined using a surface area analyzer. The maximum amount of N_2 adsorbed at a relative pressure of 0.99 defined the total pore volumes of the porous carbons. The surface areas, micropore volumes, and pore size distributions of the porous carbons were measured using the BET method, t-plot method, and DFT analysis, respectively [22]. The iodine number (mg/g carbon) of the porous carbons was measured according to the standard method [23].

The chemical compositions of materials were measured by XRF. To determine the phase compositions of the materials, XRD analysis was performed with Cu Kα1 radiation, a scanning speed of 10°/min, and operating conditions of 40 kV and 150 mA. The microstructure and micro-area composition of the materials were examined by optical microscopy and SEM-EDS. FTIR was used to analyze the functional groups of the porous carbons.

3. Results and Discussion

3.1. Effects of Reduction Temperature and Time on Properties of the Reduced Pellets and PCs

Figure 2 illustrates the impact of reduction temperature and duration on the properties of the reduced pellets and PCs. Figure 2a–c shows that as the reaction temperature rose from 1050 °C to 1250 °C, the iron grade and metallization degree of reduced pellets and the removal rate of zinc, potassium, and sodium continuously increased. This indicated that higher temperatures were advantageous for the reduction of ZD. However, when the reaction temperature exceeded 1150 °C, both the surface area and iodine number of the porous carbon materials decreased, suggesting that excessive temperatures could damage the microstructure of the carbon material.

From Figure 2d–f, the increase in the removal rate of harmful elements and iron reduction degree leveled off gradually when the reduction time reached 90 min. At a reaction temperature of 1150 °C for 90 min with a C/O molar ratio of 1.0, both the porous carbon material, which exhibited a surface area of 329.55 m^2/g and an iodine number of 667.28 mg/g, and the reduced ZDP, with an iron grade of 74.29% and an iron metallization degree of 94.88%, were obtained. Additionally, the removal rates for zinc, potassium, and sodium reached 99.24%, 95.17%, and 90.15%, respectively. However, the reduced pellets had low compressive strength and could not be used directly as burden for the blast furnace. Therefore, further optimization of the process is required.
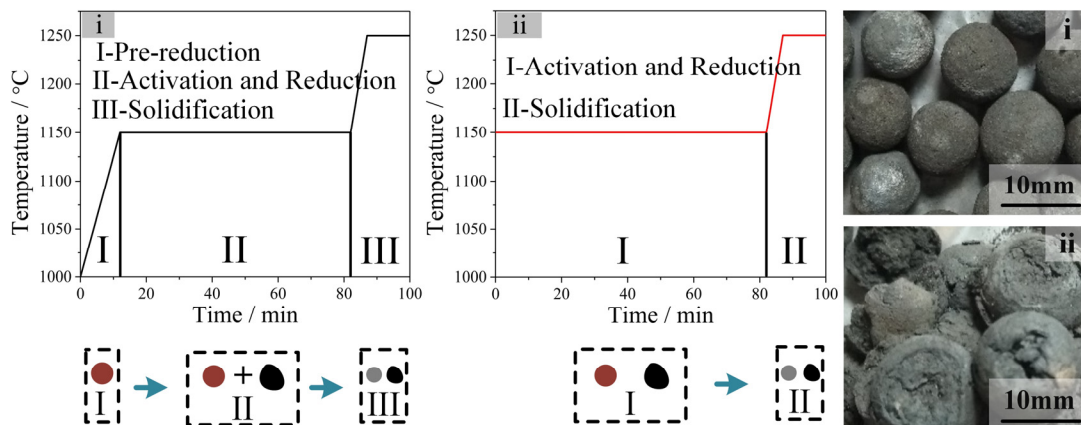
3.2. Effects of Pre-Reduction on Properties of the Reduced Pellets and PCs

Figure 3 and Table 3 illustrate the impact of the pre-reduction process on the properties of reduced ZDP. As shown in Figure 3i, the diameter of the pellets reduced from 18 mm to 10 mm following the adaptation of the pre-reduction process. However, the reduced pellets are severe in reduction swelling and reduction degradation when the dry pellets and coal directly progressed to synergistic reduction and activation stage. During the initial stage of reduction, the Fe_2O_3 in the pellets can be reduced to Fe_3O_4, and the lattice transformation can lead to a volumetric expansion of the pellets [24]. An excessive lattice

transformation rate may cause a serious reduction swelling of pellets and bring about a greater generation of irrecoverable cracks. In the pre-reduction process, the relatively low reduction temperature and C/O molar ratio could decrease the reduction rate of hematite and thus prevent the formation of cracks in the pellets.
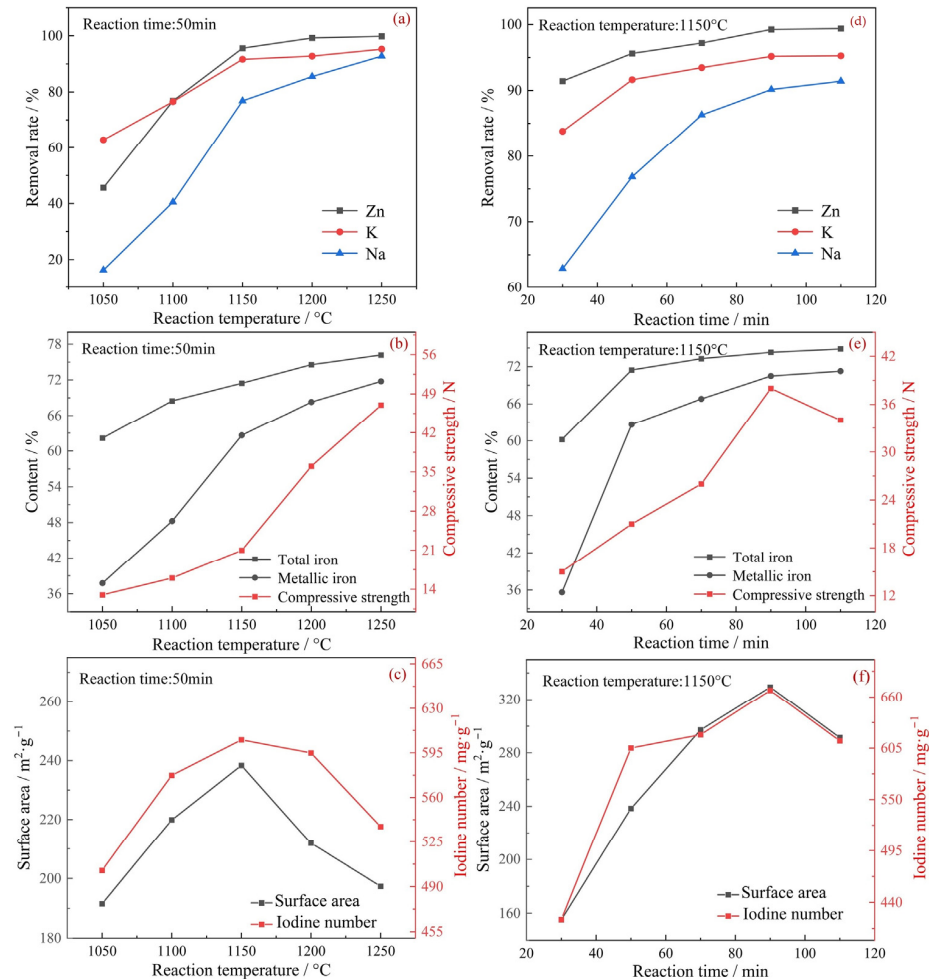
Figure 2. (**a–c**) Effects of reduction temperature on properties of the reduced pellets and PCs; (**d–f**) Effects of reduction time on properties of the reduced pellets and PCs (C/O = 1.0).

Figure 3. Effect of pre-reduction on morphology of reduced pellets. (**i**) Pre-reduced for 12 min; (**ii**) without pre-reduction.

Table 3. Effects of pre-reduction on the properties of reduced pellets.

Reduced Pellets	C/O	CCS/N per Pellet	Metallization Degree/%	Fe_{total} /%	Zn (%)	K (%)	Na (%)
Pellet (i)	1.0	856	97.83	74.27	0.010	0.007	0.023
Pellet (ii)	1.0	24	97.52	73.93	0.008	0.006	0.021
Pellet (iii)	0.5	905	97.03	73.59	0.015	0.017	0.039

Pellet (i) and pellet (iii): pre-reduced for 12 min; pellet (ii): without pre-reduction; CCS: cold compressive strength.

It can be observed from Table 3 that the reduced pellet (ii) could not be directly used as a burden for blast furnaces due to the low CCS. Pellets (i) and (iii), which possess high CCS, iron grade, and metallization degree, along with low levels of hazardous metals, can be used directly as charge to enhance blast furnace operation without needing further agglomeration.

Table 4 and Figure 4 presents the impact of the pre-reduction process on the properties of porous carbons. Part of the metal oxides was reduced by the carbon in the pellets in the pre-reduction process, and the generated CO_2 would flow out of the shaft furnace when the SC coal was added into the furnace. The surface area and iodine number of PC (i) were relatively low due to the absence of activating substance in the activation process. Increasing the mass ratio of zinc-bearing pellets to SC resulted in the formation of PC (iii), which had a surface area of 300.65 m^2/g and an iodine number of 655.23 mg/g.

**Table 4.** Effects of pre-reduction on properties of the porous carbons.

PCs	C/O	Surface Area/$m^2 \cdot g^{-1}$	Iodine Number/$mg \cdot g^{-1}$	Burn-Off/%
PC (i)	1.0	118.20	299.76	49.84
PC (ii)	1.0	134.42	601.35	55.31
PC (iii)	0.5	300.65	655.23	53.24

PC (i) and PC (iii): pre-reduced for 12 min; PC (ii): without pre-reduction.
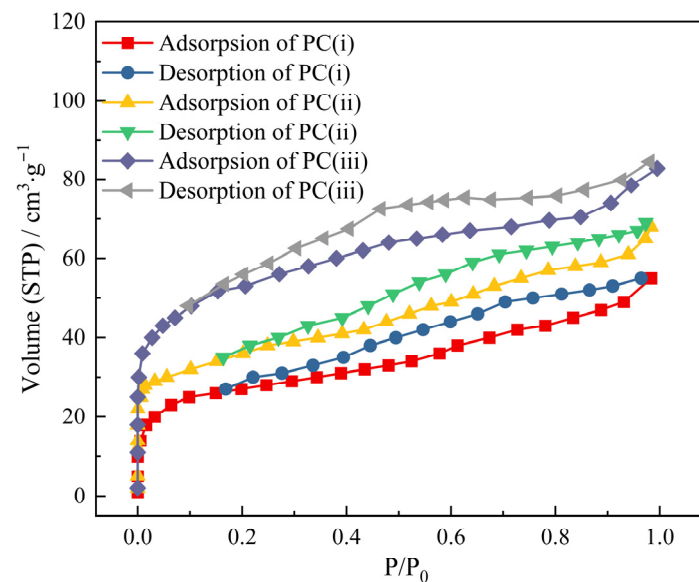
Figure 4. The N_2 adsorption–desorption isotherms of PC (i)~PC (iii).

3.3. Characterization of the Reduced Pellets and Porous Carbon Materials

The preparation conditions of the porous carbons and metallized pellets are shown in Figure 5.
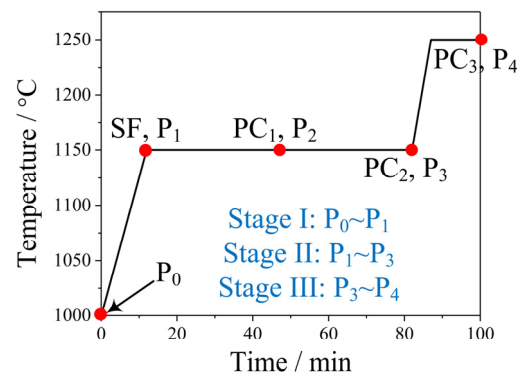
Figure 5. Preparation condition of the PCs and metallized pellets. (C/O = 0.5).

The porous carbons ($PC_1 \sim PC_3$), dry pellets (P_0) before reduction, and reduced pellets ($P_1 \sim P_4$) were fully characterized to investigate the reaction process and reveal mechanism of the synergistic reduction of metal oxides and activation of carbon.

3.3.1. Zn-Bearing Dust Pellets

Table 5 shows the properties of reduced pellets at different stages of reduction. In the pre-reduction process (stage I), significant portions of potassium and sodium were removed from the pellets and the metallization degree of the pellets increased from 2.72% to 44.31%. However, the CCS of the reduced pellets dropped from 156 Newtons per dry pellet to 45 Newtons per pellet due to the increase in the porosity of pellets resulting from the removal of volatile component. The contents of zinc, potassium, and sodium in P_3 were both lower than 0.05%, indicating that most hazardous metals were removed from the pellets at the end of the synergistic activation and reduction stage (stage II). Although the metallization degree of P_3 reached 94.55%, the CCS of P_3 was only 223 Newtons per pellet, which could not meet the requirement for blast furnace operation. The CCS of reduced pellets increased sharply, and the contents of hazardous metals further declined in the high-temperature solidification stage (stage III). Finally, the P_4 with high content and metallization degree of iron, low content of hazardous metals, and high CCS could be directly recycled as a charge to enhance blast furnace operation.

Table 5. The properties of reduced pellets (C/O = 0.5).

| Reduced Pellets	CCS/N per Pellet	Metallization Degree/%	Fe_{total} /%	Zn (%)	K (%)	Na (%)
P_0	156	2.72	35.83	3.76	1.01	0.41
P_1	45	44.31	56.55	4.23	0.57	0.32
P_2	68	91.13	72.18	0.16	0.13	0.11
P_3	223	94.55	73.22	0.039	0.023	0.042
P_4	905	97.03	73.59	0.015	0.017	0.039

CCS: Cold compressive strength.

Figure 6 illustrates the phases transformation of the ZDP during the reduction process. The diffraction peaks of P_0 indicate that the dry pellets before reduction were primarily composed of iron-bearing phases, including Fe (metallic iron), FeO (wustite), Fe_3O_4 (magnetite), and Fe_2O_3 (hematite). Phases not detected in the XRD analysis were examined using SEM/EDS analysis.
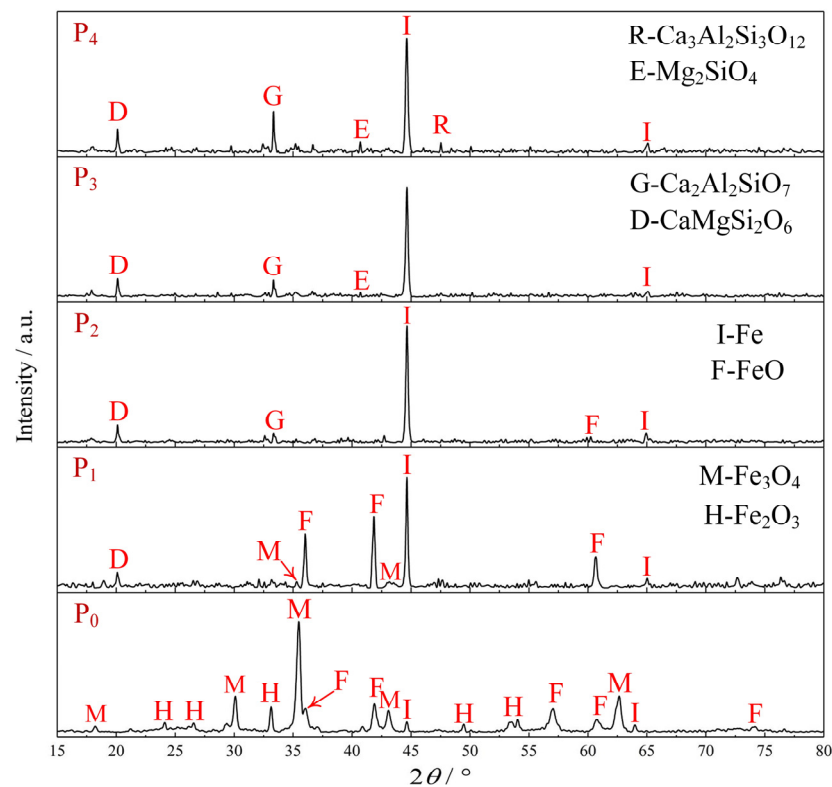
Figure 6. XRD patterns of the ZDP before and after reduction.

Figure 6 (P_1) shows that the diffraction peaks of Fe_2O_3 were negligible, while the intensities of the diffraction peaks for FeO and Fe became stronger. This indicates that most of the hematite and magnetite had been reduced to wustite and metallic iron in the pre-reduction stage. From Figure 6 (P_2 and P_3), most of the iron-bearing phases were reduced to metallic iron after stage II. The gangue phases, which included $CaMgSi_2O_6$ (diopside), $Ca_2Al_2SiO_7$ (gehlenite), and Mg_2SiO_4 (forsterite), were gradually generated as the reaction progress and formation of $Ca_3Al_2Si_3O_{12}$ (grossular) required the higher temperature.

Figure 7a presents the optical micrograph of P_0 and the electronic micrographs in Figure 7b,c. Table 6 provides the elemental compositions of the micro-areas shown in Figure 7. From point 1 in Figure 7b, a small amount of metallic iron grains existed in the ZD before reduction. The spherical particle (point 2) with a size of 80 microns consisted of Fe_3O_4 (magnetite).
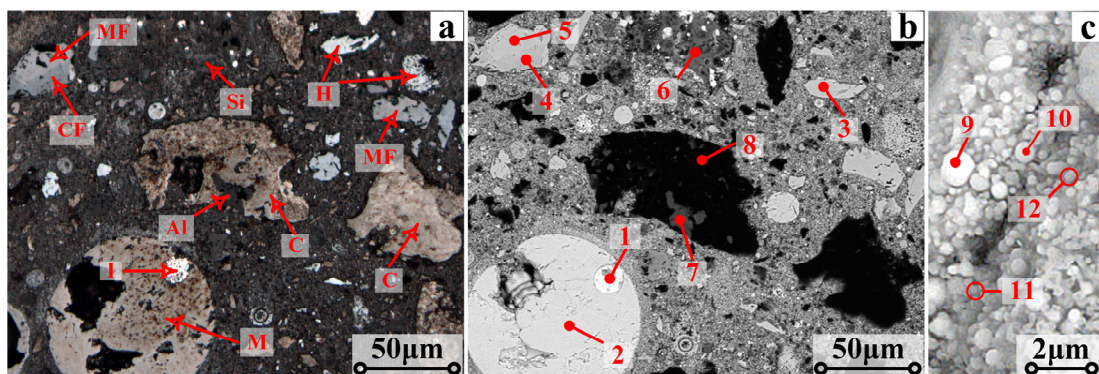
Figure 7. The optical micrograph (**a**) and electronic micrograph (**b**,**c**) of the pellets before reduction. (I—Fe-metallic iron, H—Fe_2O_3-hematite, M—Fe_3O_4-magnetite, CF—$CaFe_2O_4$-calcium ferrite, MF—$MgFe_2O_4$-magnesioferrite, Al—Al_2O_3-alumina, Si—SiO_2-silica, C—carbon).

Table 6. Compositions of the zinc-bearing dust pellets before reduction (EDS analysis, points on Figure 7, atomic conc, %).

| Point No.	Elements										Possible Phases
	Fe	O	Si	Ca	Mg	Al	Zn	K	Na	C	
1	100	0	0	0	0	0	0	0	0	0	Fe
2	41.3	58.7	0	0	0	0	0	0	0	0	Fe_3O_4
3	40.5	59.5	0	0	0	0	0	0	0	0	Fe_2O_3
4	29.3	56.9	0	13.8	0	0	0	0	0	0	$CaFe_2O_4$
5	29.7	57.7	0	0	12.6	0	0	0	0	0	$MgFe_2O_4$
6	0	67.9	32.1	0	0	0	0	0	0	0	SiO_2
7	0	61.6	0	0	0	38.4	0	0	0	0	Al_2O_3
8	0	0	0	0	0	0	0	0	0	100	C
9	29.8	58.1	0	0	0	0	12.1	0	0	0	$ZnFe_2O_4$
10	40.2	59.8	0	0	0	0	0	0	0	0	Fe_2O_3
11	36.7	57.7	0	0	0	0	0	0	5.6	0	$NaFeO_2$, Fe_2O_3
12	37.1	56.5	0	0	0	0	0	6.4	0	0	$KFeO_2$, Fe_2O_3

It was observed that part of the Fe_2O_3 (hematite) (point 3) was presented as agglomerates with a particle size ranging from 10 to 25 microns, while other hematite particles with an average particle size of less than 2 microns (point 10) were distributed around the agglomerates. The calcium, magnesium, silicon, and aluminum existed in $CaFe_2O_4$ (calcium ferrite), $MgFe_2O_4$ (magnesioferrite), SiO_2 (silica), and Al_2O_3 (alumina), respectively (points 4~7). The black regions in Figure 7b consisted of carbon, which can generate CO that subsequently reacts with the metal oxides in the pellets. The zinc existed in spherical $ZnFe_2O_4$ (zinc ferrite) grains with a size of 1 micron (point 9). From points 11 and 12 in Figure 7c, the atomic contents of sodium and potassium were only 5.6% and 6.4%, respectively, indicating that these particles consisted of the solid solution of $NaFeO_2$/$KFeO_2$ and Fe_2O_3. Figure 7 illustrates the microstructure and phase transformation of the reduced pellets in the reduction process. The elementary compositions of micro-areas shown in Figure 7 are detailed in Table 7.

Table 7. Compositions of the zinc-bearing dust pellets after reduction (EDS analysis, points on Figure 5, atomic conc, %).

Point No.	Elements									Possible Phases
	Fe	O	Si	Ca	Mg	Al	Zn	K	Na	
1	100	0	0	0	0	0	0	0	0	Fe
2	51.2	48.8	0	0	0	0	0	0	0	FeO
3	45.8	43.9	0	0	0	0	10.3	0	0	$ZnFe_2O_4$, Fe
4	85.4	11.1	0	0	0	0	0	0	3.5	$NaFeO_2$, Fe
5	88.9	8.8	0	0	0	0	0	2.3	0	$KFeO_2$, Fe
6	0	60.4	24.3	8.7	6.6	0	0	0	0	$CaMgSi_2O_6$
7	91.3	7.3	0	0	0	0	1.4	0	0	$ZnFe_2O_4$, Fe
8	93.6	4.8	0	0	0	0	0	0	1.6	$NaFeO_2$, Fe
9	96.3	3.1	0	0	0	0	0	0.6	0	$KFeO_2$, Fe
10	0	62.0	8.4	15.9	0	13.7	0	0	0	$Ca_2Al_2SiO_7$
11	0	60.5	21.1	10.5	7.9	0	0	0	0	$CaMgSi_2O_6$
12	35.2	52.2	0	0	12.6	0	0	0	0	$MgFe_2O_4$
13	0	57.8	17.3	16.3	0	8.6	0	0	0	$Ca_3Al_2Si_3O_{12}$

From Figure 8 (P_1), certain amounts of metallic iron (point 1) and wustite (point 2) could be observed in the pre-reduced pellets. The atomic content of zinc in point 3 was found to be 10.3%, which was lower than that of pure $ZnFe_2O_4$, indicating that part of the zinc ferrite was reduced to metallic iron and gaseous zinc in the pre-reduction stage. Similarly, it can be seen from points 4 and 5 that parts of the potassium iron oxide and sodium iron oxide were reduced in stage I. The porosity of the pellets increased due to the

removal of volatile components from the pellets, leading to the strength degradation of the pellets.
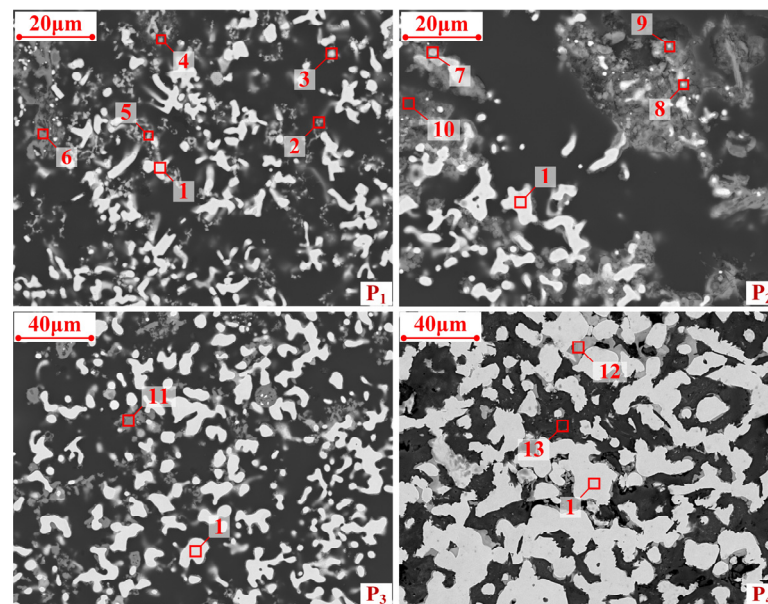
Figure 8. SEM images of the reduced pellets.

From Figure 8 (P_2), most of the fine-grained wustite vanished from the pellets, while zinc ferrite, potassium iron oxide, and sodium iron oxide (point 7, 8 and 9) were still present in the reduced pellets. As shown in Figure 8 (P_3), most of the harmful elements had been removed, and there is a noticeable increase in the size of the metallic iron grains after stage II. However, the CCS of the P_3 was still low (223 Newtons per pellets) due to the dispersion state of metallic iron grains. After the solidification stage, the phases in P_4 were interconnected by metallic iron and magnesioferrite (point 12). With the increase in metallic iron grains, the CCS of the reduced pellets rose from 223 to 905 Newtons per pellet. Reduced pellets with good strength can be used directly as charge to enhance blast furnace operation, without the need for additional agglomeration. The SEM/EDS analyses were consistent with the results of XRD analysis.

3.3.2. Porous Carbon Materials

Figure 9i illustrates nitrogen adsorption–desorption isotherms of PCs at 77 K. The dramatic increase in the adsorption curves at a relative pressure of $P/P_0 < 0.1$ indicated that the carbon materials have a high content of micropores, and the micropore contents of PC_1 were lower than those of PC_2 and PC_3. The hysteresis loop in the range of $0.3 < P/P_0 < 0.95$ confirmed the presence of certain amounts of mesopores in the carbon materials [25], and the hysteresis loop of PC_3 possessed a larger area due to the relatively high proportion of mesopores.

According to the IUPAC classification [26,27], the adsorption–desorption isotherms fall under a combination of type I and type IV, indicating a structure that includes both micropores and mesopores. The pore size distribution and surface areas of PCs are shown in Figure 9ii and Table 8. PC_1 exhibited a surface area of 218.9 m^2/g, a total pore volume of 0.191 mL/g, and a micropore content of 52.37%. Figure 9 shows that increasing the activation time significantly elevated the surface area and pore volume of the carbon material. The excessive temperature in stage III caused a small portion of the microporous structure of the carbon material to break down. Ultimately, PC_3 demonstrated a surface area of 300.7 m^2/g, a total pore volume of 0.264 mL/g, and a micropore content of 48.21%. Although the surface area of P_3 was lower than that of activated carbons in other studies [28,29], the porous carbon produced as a

byproduct of the process can enhance the economic benefit and energy efficiency of the ZD disposal process.
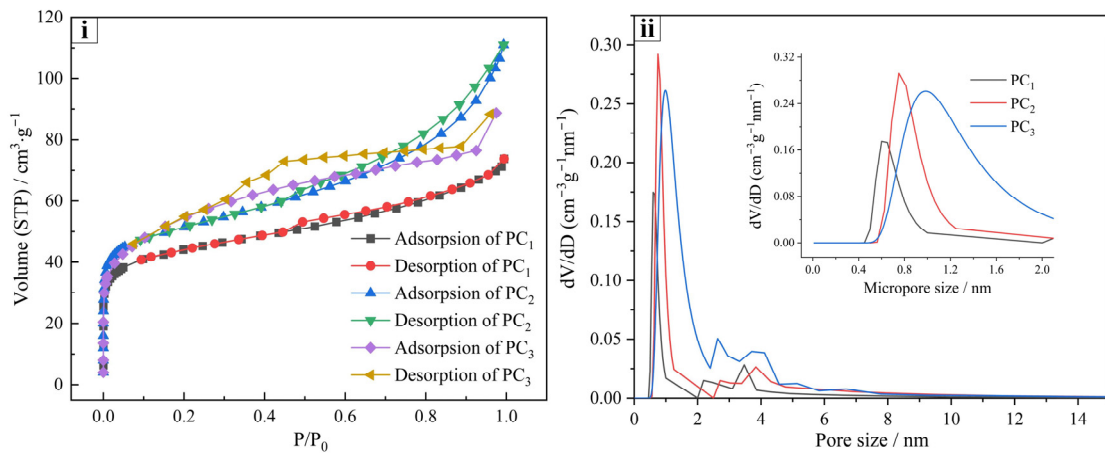

Figure 9. (**i**) N_2 adsorption–desorption isotherms; (**ii**) Pore size distributions of PCs.

Table 8. Surface areas and porosities of the PCs.

Samples	Surface Area (m^2/g)	Total Pore Volume (mL/g)	Micropore (<2 nm)		Mesopore	
			Volume (mL/g)	Percentage (%)	Volume (mL/g)	Percentage (%)
PC_1	218.9	0.191	0.100	52.37	0.091	47.63
PC_2	314.8	0.273	0.135	49.63	0.138	50.37
PC_3	300.65	0.264	0.127	48.21	0.137	51.79

Figure 10 illustrates the microstructure transformation of porous carbon material during the reduction and activation processes. It can be observed that the surface of PC_2 presented an apparent microporous structure, while the porosity of PC_1 was significantly less than that of PC_2. Pores formed continuously as tarry substances were removed and carbon underwent gasification in stage II. However, some micropores collapsed and more mesopores were formed at high temperatures in stage III. The scanning electron microscopy analysis aligned with the findings from the N_2 adsorption–desorption analysis.
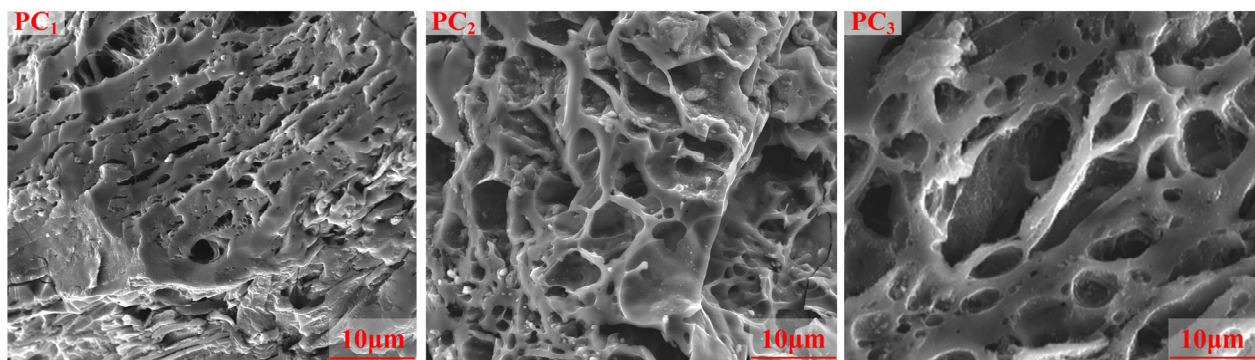

Figure 10. SEM images of PCs.

The main elements distribution in PC_3 is shown in Figure 11. It can be observed that potassium and sodium were adsorbed onto the carbon skeleton, with their positional distribution aligning with that of oxygen, indicating that the K and Na elements in the porous carbon material were present as potassium oxide and sodium oxide, respectively. $KFeO_2$ and $NaFeO_2$ in the dust can be reduced to gaseous metal potassium and sodium,

which are adsorbed by the porous carbon material. The contents of K_2O, Na_2O, and ZnO in PC_3 were found at 0.76%, 0.47%, and 0.03%, respectively.
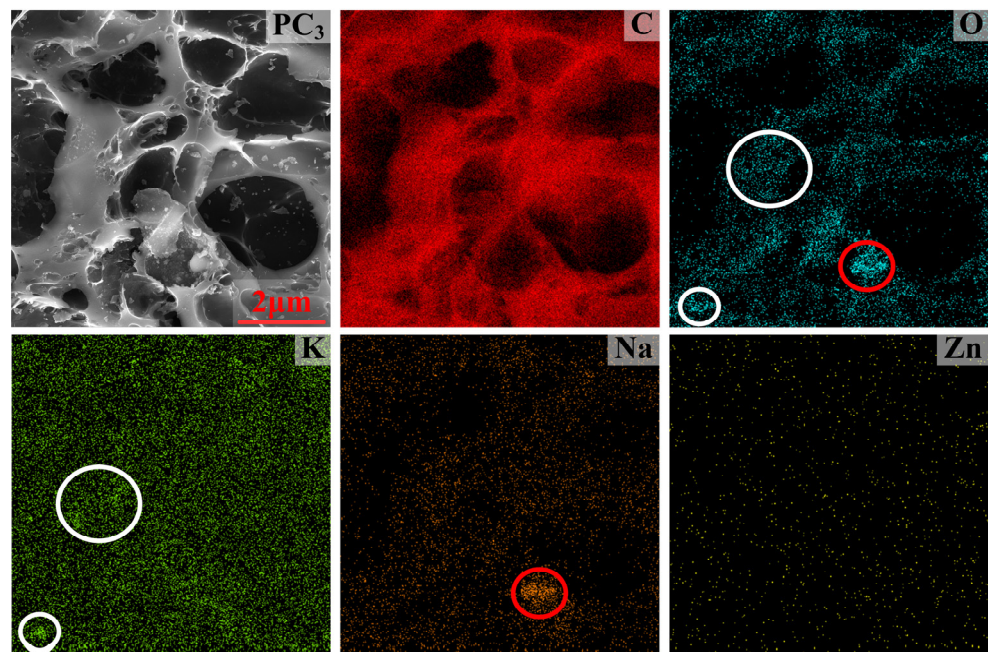
Figure 11. Elements distribution in PC_3.

To investigate the functional groups on the surface of the carbon materials, the infrared spectra of $PC_1\sim PC_3$ were analyzed. The results are presented in Figure 12.
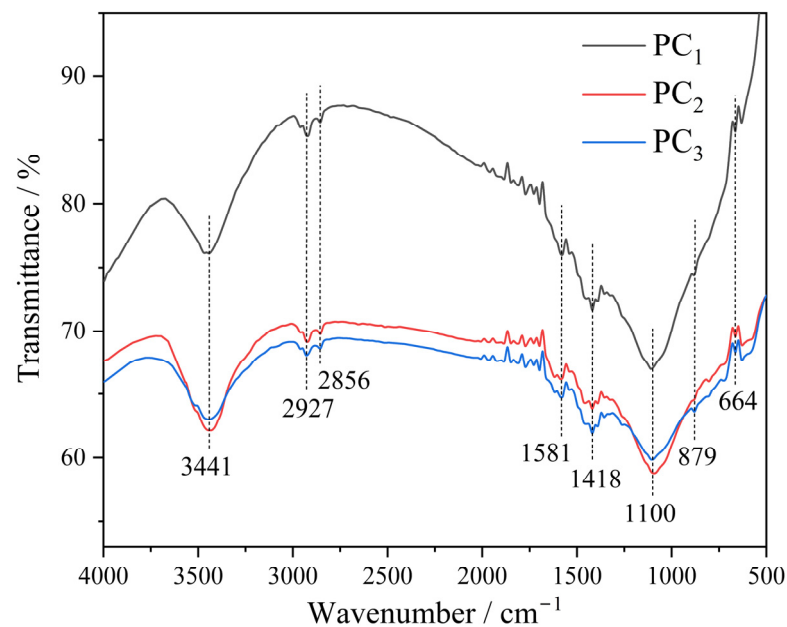
Figure 12. Fourier transform infrared spectroscopy (FTIR) spectra of PCs.

The three spectra showed a similar shape, while the transmittance of PC_1 was obviously higher than that of PC_2 and PC_3, which was probably due to the incomplete activation of PC_1. The strong and broad bands observed at 3441 cm^{-1} were attributed to the stretching vibration of the hydroxyl functional group (O-H) [30,31]. The bands at 2927 cm^{-1} and its shoulder at 2856 cm^{-1} were ascribed to the stretching and bending vibration of C–H bands, respectively [32]. The bands at 1581 cm^{-1} can be assigned to the stretching vibrations

of C=C [33]. The bands at 1418 cm^{-1} were related to some oxygen-bearing groups like ketones and carboxyl [34]. The bands at 1100 cm^{-1} were attributed to C–O–C stretching, while the bands at 879 and 664 cm^{-1} were related to out-of-plane bending in benzene derivatives [33].

In the steel manufacturing process, approximately 70% of SO_2 and 40% of NOx are produced during the sintering process [35]. Therefore, removing SO_2 and NOx from the sintering flue gas is essential. Currently, many steel plants have widely adopted activated carbon adsorption methods to purify the sintering flue gas [36].

Figure 13 shows the desulfurization and denitration performances of PC_3 and the commercial activated carbon (CAC), which is applied to the sintering flue gas purifying process in Bao steel of China. The adsorption capacities for sulfur dioxide were 5.91 mg/g for PC_3 and 5.48 mg/g for CAC. The adsorption capacities for nitric oxide were 1.19 mg/g for PC_3 and 1.07 mg/g for CAC. The removal rates of SO_2 and NO could reach 98% and 62%, respectively, which were higher than those in some previous studies [37–39]. Despite PC_3 having a relatively low surface area [40], the presence of alkaline oxides (K_2O and Na_2O) and functional groups enhanced its adsorption of acid gases (SO_2 and NO). PC_3 demonstrated higher desulfurization and denitration efficiency compared to CAC, indicating that PC_3 is more effective at disposing SO_2 and NO-containing flue gas.

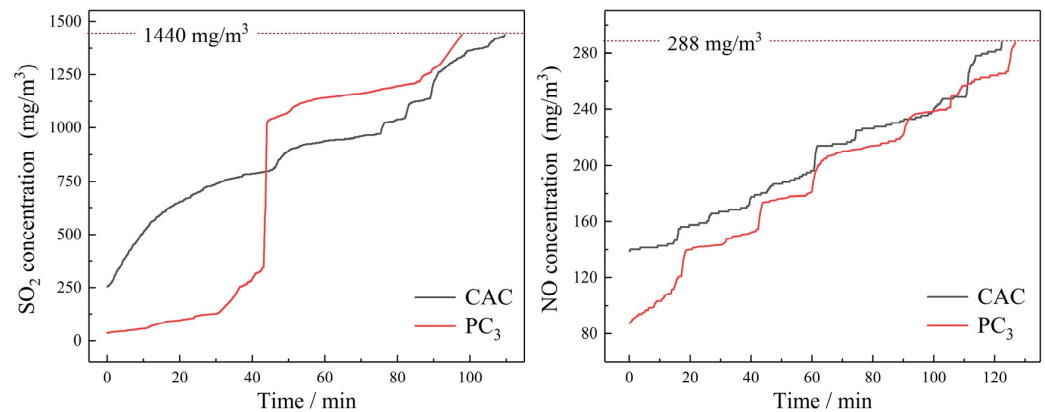**Figure 13.** The SO_2/NO breakthrough curves of the carbon materials at 80 °C.

3.4. Mechanism of the Synergistic Reduction and Activation

Figure 14 illustrates the mechanism of synergistic reduction and activation, with the chemical reactions (1)~(12) involved listed in Table 9.
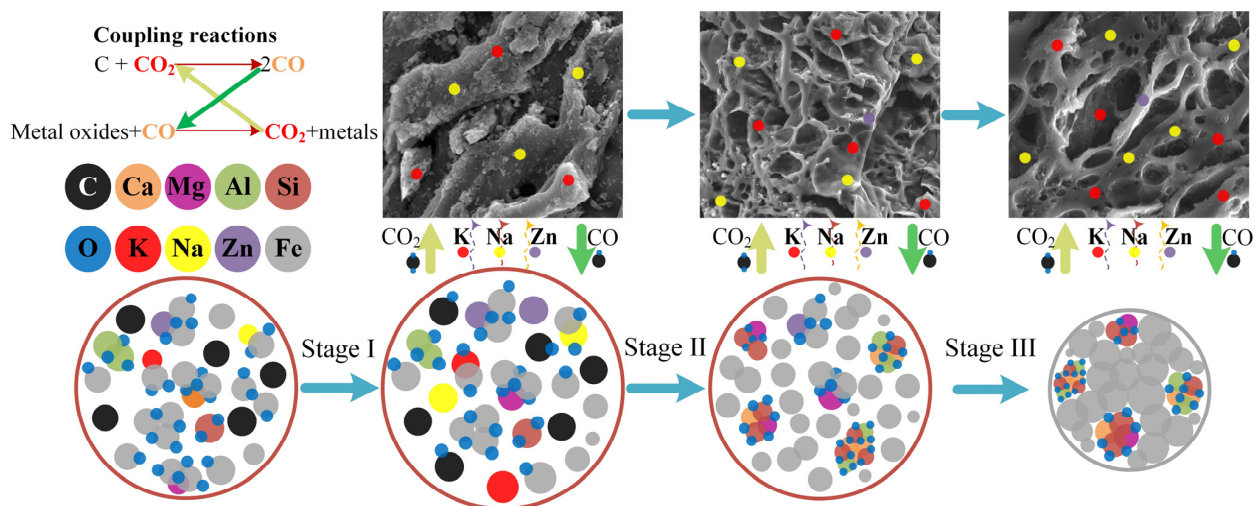

Figure 14. Schematic diagram of the mechanism of synergistic reduction and activation.

Table 9. The main reactions present in the reduction and activation process.

NO.	Reaction Types	Reactions
(1)	Activation reaction, Boudouard reaction	$C + CO_2 \rightarrow 2CO$
(2)		$3Fe_2O_3 + CO \rightarrow 2Fe_3O_4 + CO_2$
(3)		$Fe_3O_4 + CO \rightarrow 3FeO + CO_2$
(4)	Reduction reactions of iron-bearing phases	$FeO + CO \rightarrow Fe + CO_2$
(5)		$CaFe_2O_4 + 3CO \rightarrow CaO + 2Fe + 3CO_2$
(6)		$MgFe_2O_4 + 3CO \rightarrow MgO + 2Fe + 3CO_2$
(7)		$ZnFe_2O_4 + 4CO \rightarrow Zn + 2Fe + 4CO_2$
(8)	Reduction reactions of harmful metal oxides	$KFeO_2 + 2CO \rightarrow Fe + 2CO_2 + K$
(9)		$NaFeO_2 + 2CO \rightarrow Fe + 2CO_2 + Na$
(10)		$2CaO + SiO_2 + Al_2O_3 \rightarrow Ca_2Al_2SiO_7$
(11)	Reactions of gangue phases	$CaO + 2SiO_2 + MgO \rightarrow CaMgSi_2O_6$
(12)		$3CaO + 3SiO_2 + Al_2O_3 \rightarrow Ca_3Al_2Si_3O_{12}$

The thermodynamic analysis of these reactions was carried out through Factsage7.1 to investigate their initial reaction temperatures, and the results are presented in Figure 15. Figure 15B shows that the initial reduction temperatures for iron oxides, including hematite, magnetite, wustite, calcium ferrite, and magnesioferrite, were all below 750 °C. In contrast, the initial reduction temperatures for zinc ferrite, potassium iron oxide, and sodium iron oxide were significantly higher, at 908 °C, 939 °C, and 948 °C, respectively. The operation temperatures in this paper were 1150~1250 °C, which were higher than the initial reaction temperatures of the chemical reactions in Table 9. From reactions (2)~(9) in Table 9, metal oxides in ZDP could be reduced by CO to produce CO_2. In the meantime, the carbon in the coal could be activated by CO_2 generated from these reduction reactions, and the CO generated from the activation reaction (reaction (1) in Table 9) could facilitate the reduction reactions in return. Therefore, the reduction of metal oxides in ZDP and the activation of carbon in coal were mutually enhanced through these coupling reactions. In addition, the carbon cycle between the coal and dusts could decrease the carbon emission. The in-depth analysis of the carbon cycle in this process and utilization of cleaner materials like biomass will be studied in our further investigation.
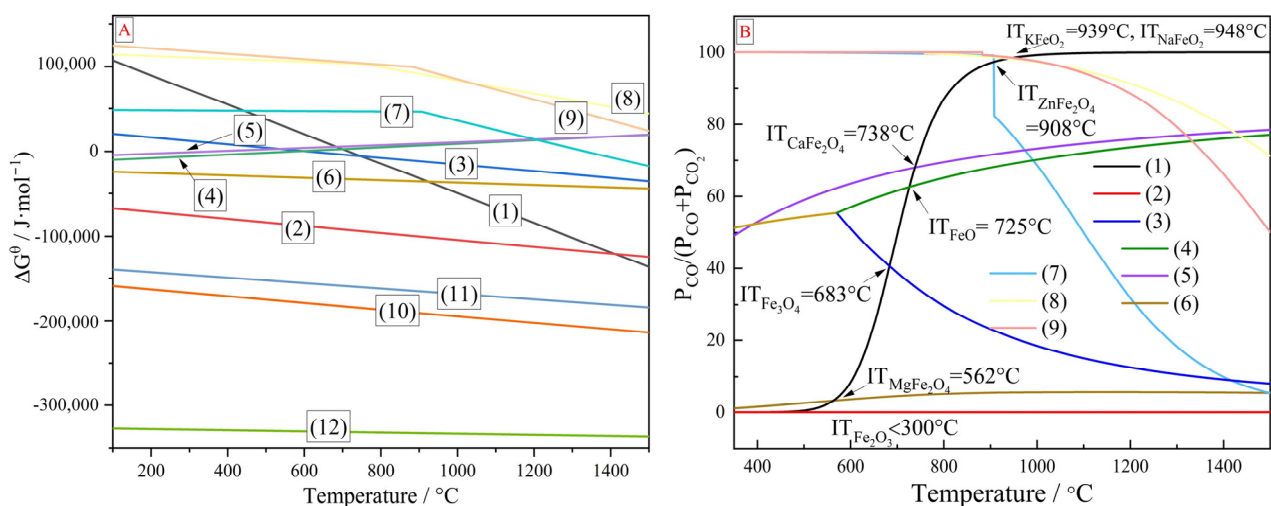
Figure 15. (**A**) Standard Gibbs free energy ΔG^θ vs. reaction temperature for the reactions (1)~(12) in Table 9; (**B**) Equilibrium composition of gas phases vs. reaction temperature for the reactions (1)~(9) in Table 9 (IT-initial reaction temperature).

It can be seen from Figure 14 that the carbon in the pellets reacted with oxygen and existed in the pellets to form carbon monoxide at the beginning of the pre-reduction process

(stage I). Subsequently, the carbon monoxide reacted with nearby metal oxides to produce carbon dioxide. This carbon dioxide then reacted with carbon to generate a reducing gas via the Boudouard reaction [41,42]. These coupling reactions only occurred inside the pellets in stage I. Most of the Fe_2O_3 and Fe_3O_4 were reduced to FeO, leading to volume expansion of the pellets in stage I. The porosity of the pellets increased with the removal of volatile components and volume expansion, which was beneficial for the diffusion of the gases (CO, CO_2, Zn, K, and Na). After stage I, the SC coal was added into the furnace, and the coupling reactions were performed between the coal and ZDP. In stage II, the CO produced from the coal activation reaction reduced most of the iron-bearing phases. The strength of the pellets remained low due to the dispersed distribution of metallic iron grains. The vast majority of Zn, K, and Na were removed from the pellets, and considerable amounts of the K and Na, which have a catalytic effect on carbon activation, were absorbed by the porous carbon in the synergistic reduction and activation stage [16,17]. The coal was transferred into the porous carbon material with abundant functional groups and micropores after stage II. In the solidification stage (stage III), almost all the reducible metal oxides had been reduced, and the absence of an activator quenched the chain reactions. Under high-temperature conditions, the metallic iron grains bonded with each other, significantly increasing the strength of the reduced pellets. Finally, the coal was activated by the ZD and transferred into porous carbon material, which can be used to purify the sintering flue gas, while the ZDP were reduced to metallized pellets, which can be directly used as burden to enhance blast furnace operation.

4. Conclusions

A process for utilization of ZD and low-rank coal was developed, through which not only the dusts were reduced to the high-quality blast furnace burden but also a low-rank could be transferred into high-value porous carbon material simultaneously. The mechanism of the process of synergistic reduction of metal oxides and activation of carbon was clarified. The conclusions can be drawn as follows:

(1) The reduced zinc-bearing dust pellets with CCS of 905 Newtons per pellet, iron grade of 73.59%, iron metallization degree of 97.03%, and low content of hazardous metals (0.015% Zn, 0.017% K, and 0.039% Na) could be directly used as burden for improving blast furnace operations without further agglomeration.

(2) Although the surface area of the porous carbon was not high, it possessed better SO_2 and NO adsorption capacities compared with the commercial activated carbon due to abundant functional groups and considerable amounts of alkaline oxides (0.76% K_2O and 0.47% Na_2O) in the material.

(3) In the synergistic reduction and activation process, the Fe_2O_3, Fe_3O_4, FeO, $ZnFe_2O_4$, $MgFe_2O_4$, $CaFe_2O_4$, $KFeO_2$, and $NaFeO_2$ in Zn-bearing pellets could be reduced by the CO, which was generated from the activation reaction of coal, while the coal was activated by the CO_2 generated from the reduction reactions. The synchronous reduction and activation processes were promoted by the coupling reactions between the Zn-bearing dust pellets and coal.

Author Contributions: Conceptualization, D.W., D.Z. and J.Y.; methodology, D.W. and D.Z.; writing—original draft preparation, D.W.; writing—review and editing, D.W.; investigation, D.W.; visualization, D.W. and S.M.; resources, S.M. and D.Z.; supervision, S.M.; formal analysis, D.Z. and J.Y.; project administration, J.Y. All authors have read and agreed to the published version of the manuscript.

Institutional Review Board Statement: Not applicable.

Informed Consent Statement: Informed consent was obtained from all subjects involved in the study.

Data Availability Statement: The data presented in this study are available on request from the corresponding author. The data are not publicly available due to institutional policies that restrict data sharing.

Conflicts of Interest: The authors declare no conflict of interest.

References

1. Li, H.; Pinson, D.J.; Zulli, P.; Lu, L.; Longbottom, R.J.; Chew, S.J.; Monaghan, B.J.; Zhang, G. Zinc Removal from Basic Oxygen Steelmaking (BOS) Filter Cake by Sintering. *J. Hazard. Mater.* **2020**, *385*, 121592. [CrossRef] [PubMed]
2. Chairaksa-Fujimoto, R.; Inoue, Y.; Umeda, N.; Itoh, S.; Nagasaka, T. New Pyrometallurgical Process of EAF Dust Treatment with CaO Addition. *Int. J. Miner. Metall. Mater.* **2015**, *22*, 788–797. [CrossRef]
3. Guo, Z.; Xu, X.; Li, S.; Zhu, D.; Pan, J.; Yang, C. Hydrogen Reduction Process for Zinc-Bearing Dust Treatment: Reduction Kinetic Mechanism and Microstructure Transformations in a Novel and Environmentally Friendly Metallurgical Technique. *J. Environ. Chem. Eng.* **2023**, *11*, 110836. [CrossRef]
4. Fan, C.; Ding, C.; Wang, X.; Xue, S.; Chang, R.; Long, H. A Novel Resource Recovery Strategy: Substituting Carbon Powder with Organic Solid Waste in the Production of Zinc-Bearing Dust Sludge Metallization Pellets. *Powder Technol.* **2024**, *448*, 120328. [CrossRef]
5. Qi, L.; Wei, R.; Wang, Y.; Long, H.; Charles Xu, C. A New Approach to Collaborative Resource Utilization of Biological Sludge and Zinc-Bearing Dust: Reduction Characteristics and Mechanisms. *Sep. Purif. Technol.* **2025**, *357*, 130102. [CrossRef]
6. Xia, L.; Mao, R.; Zhang, J.; Xu, X.; Wei, M.; Yang, F. Reduction Process and Zinc Removal from Composite Briquettes Composed of Dust and Sludge from a Steel Enterprise. *Int. J. Miner. Metall. Mater.* **2015**, *22*, 122–131. [CrossRef]
7. She, X.; Wang, J.; Wang, G.; Xue, Q.; Zhang, X. Removal Mechanism of Zn, Pb and Alkalis from Metallurgical Dusts in Direct Reduction Process. *J. Iron Steel Res. Int.* **2014**, *21*, 488–495. [CrossRef]
8. Wang, D.; Zhu, D.; Pan, J.; Guo, Z.; Yang, C.; Wang, X.; Dong, T. An Investigation into the Alkali Metals Removal from Zn-Bearing Dust Pellets in Direct Reduction. *JOM* **2022**, *74*, 634–643. [CrossRef]
9. Zhang, W.; Dong, T.; Zhu, D.; Jiang, Y.; Pan, J.; Guo, Z.; Li, S.; Ma, W. Improving Zinc Reduction and Removal from Pellets of Zinc-Bearing Dusts via Vacuum Microwave-Assisted Carbothermal Reduction Process. *Process Saf. Environ. Prot.* **2024**, *192*, 896–906. [CrossRef]
10. Wu, L.; Mei, H.; Liu, K.; Lv, N.; Wang, H.; Dong, Y. The Behavior of Separation and Enrichment of Valuable Metals during the Synergistic Processing of Metallurgical Dust and Sludge via Roasting in Rotary Kiln. *J. Environ. Chem. Eng.* **2023**, *11*, 109473. [CrossRef]
11. Reddy, A.L.S.B.; Sahoo, S.K.; Kumar, M. Studies on Characterization of Properties of Low-Grade Hematite Iron Ores and Their Fired Pellets. *Ironmak. Steelmak.* **2023**, *50*, 1215–1223. [CrossRef]
12. Krauklis, A.E.; Karl, C.W.; Gagani, A.I.; Jørgensen, J.K. Composite Material Recycling Technology—State-of-the-Art and Sustainable Development for the 2020s. *J. Compos. Sci.* **2021**, *5*, 28. [CrossRef]
13. Ji, P.; Bing, P.; Di, Y.; Mo-tang, T.A. Kinetics of Isothermal Reduction of Stainless Steelmaking Dust Pellets①. *Trans. Nonferrous Met. Soc. China* **2004**, *14*, 593–598.
14. Zabaniotou, A.; Madau, P.; Oudenne, P.D.; Jung, C.G.; Delplancke, M.-P.; Fontana, A. Active Carbon Production from Used Tire in Two-Stage Procedure: Industrial Pyrolysis and Bench Scale Activation with H_2O–CO_2 Mixture. *J. Anal. Appl. Pyrolysis* **2004**, *72*, 289–297. [CrossRef]
15. Alam, S.; Khan, M.S.; Bibi, W.; Zekker, I.; Burlakovs, J.; Ghangrekar, M.M.; Bhowmick, G.D.; Kallistova, A.; Pimenov, N.; Zahoor, M. Preparation of Activated Carbon from the Wood of Paulownia Tomentosa as an Efficient Adsorbent for the Removal of Acid Red 4 and Methylene Blue Present in Wastewater. *Water* **2021**, *13*, 1453. [CrossRef]
16. Pezoti, O.; Cazetta, A.L.; Bedin, K.C.; Souza, L.S.; Martins, A.C.; Silva, T.L.; Santos Júnior, O.O.; Visentainer, J.V.; Almeida, V.C. NaOH-Activated Carbon of High Surface Area Produced from Guava Seeds as a High-Efficiency Adsorbent for Amoxicillin Removal: Kinetic, Isotherm and Thermodynamic Studies. *Chem. Eng. J.* **2016**, *288*, 778–788. [CrossRef]
17. Basta, A.H.; Fierro, V.; El-Saied, H.; Celzard, A. 2-Steps KOH Activation of Rice Straw: An Efficient Method for Preparing High-Performance Activated Carbons. *Bioresour. Technol.* **2009**, *100*, 3941–3947. [CrossRef]
18. Huo, Q.; Li, J.; Qi, X.; Liu, G.; Zhang, X.; Zhang, B.; Ning, Y.; Fu, Y.; Liu, J.; Liu, S. Cu, Zn-Embedded MOF-Derived Bimetallic Porous Carbon for Adsorption Desulfurization. *Chem. Eng. J.* **2019**, *378*, 122106. [CrossRef]
19. Damdin, B.; Barnasan, P.; Lin, C.-J.; Sanjaa, B.; Alyeksandr, A. Preparation and Characterization of Activated Carbons from Different Kinds of Coal. *Proc. Mong. Acad. Sci.* **2020**, *60*, 25–31. [CrossRef]
20. Gornostayev, S.S.; Heikkinen, E.; Heino, J.J.; Huttunen, S.M.M.; Fabritius, T.M.J. Behavior of Alkali-Bearing Minerals in Coking and Blast Furnace Processes. *Steel Res. Int.* **2016**, *87*, 1144–1153. [CrossRef]
21. Zhu, D.; Wang, D.; Pan, J.; Guo, Z.; Yang, C. Utilization of Hydrated Lime as Binder and Fluxing Agent for the Production of High Basicity Magnesium Fluxed Pellets. *ISIJ Int.* **2022**, *62*, 632–641. [CrossRef]
22. Landers, J.; Gor, G.Y.; Neimark, A.V. Density Functional Theory Methods for Characterization of Porous Materials. *Colloids Surf. A Physicochem. Eng. Asp.* **2013**, *437*, 3–32. [CrossRef]

23. Hsieh, C.-T.; Teng, H. Influence of Mesopore Volume and Adsorbate Size on Adsorption Capacities of Activated Carbons in Aqueous Solutions. *Carbon* **2000**, *38*, 863–869. [CrossRef]

24. Wang, D.; Pan, J.; Zhu, D.; Guo, Z.; Yang, C.; Yuan, Z. An Efficient Process to Upgrade Siderite Ore by Pre Oxidation-Magnetization Roasting-Magnetic Separation-Acid Leaching. *J. Mater. Res. Technol.* **2022**, *19*, 4296–4307. [CrossRef]

25. Konikkara, N.; Kennedy, L.J.; Vijaya, J.J. Preparation and Characterization of Hierarchical Porous Carbons Derived from Solid Leather Waste for Supercapacitor Applications. *J. Hazard. Mater.* **2016**, *318*, 173–185. [CrossRef]

26. Sudaryanto, Y.; Hartono, S.B.; Irawaty, W.; Hindarso, H.; Ismadji, S. High Surface Area Activated Carbon Prepared from Cassava Peel by Chemical Activation. *Bioresour. Technol.* **2006**, *97*, 734–739. [CrossRef]

27. Balbuena, P.B.; Gubbins, K.E. Theoretical Interpretation of Adsorption Behavior of Simple Fluids in Slit Pores. *Langmuir* **1993**, *9*, 1801–1814. [CrossRef]

28. Bashkova, S.; Bandosz, T.J. The Effects of Urea Modification and Heat Treatment on the Process of NO2 Removal by Wood-Based Activated Carbon. *J. Colloid. Interface Sci.* **2009**, *333*, 97–103. [CrossRef] [PubMed]

29. Veksha, A.; Sasaoka, E.; Uddin, M.D.A. The Influence of Porosity and Surface Oxygen Groups of Peat-Based Activated Carbons on Benzene Adsorption from Dry and Humid Air. *Carbon* **2009**, *47*, 2371–2378. [CrossRef]

30. Chen, C.; Kim, J.; Ahn, W.-S. Efficient Carbon Dioxide Capture over a Nitrogen-Rich Carbon Having a Hierarchical Micro-Mesopore Structure. *Fuel* **2012**, *95*, 360–364. [CrossRef]

31. Alabadi, A.; Abbood, H.A.; Li, Q.; Jing, N.; Tan, B. Imine-Linked Polymer Based Nitrogen-Doped Porous Activated Carbon for Efficient and Selective CO2 Capture. *Sci. Rep.* **2016**, *6*, 38614. [CrossRef] [PubMed]

32. Zahoor, M.; Ullah, A.; Alam, S.; Muhammad, M.; Hendroko Setyobudi, R.; Zekker, I.; Sohail, A. Novel Magnetite Nanocomposites (Fe3O4/C) for Efficient Immobilization of Ciprofloxacin from Aqueous Solutions through Adsorption Pretreatment and Membrane Processes. *Water* **2022**, *14*, 724. [CrossRef]

33. Deng, H.; Li, G.; Yang, H.; Tang, J.; Tang, J. Preparation of Activated Carbons from Cotton Stalk by Microwave Assisted KOH and K2CO3 Activation. *Chem. Eng. J.* **2010**, *163*, 373–381. [CrossRef]

34. Foo, K.Y.; Hameed, B.H. Textural Porosity, Surface Chemistry and Adsorptive Properties of Durian Shell Derived Activated Carbon Prepared by Microwave Assisted NaOH Activation. *Chem. Eng. J.* **2012**, *187*, 53–62. [CrossRef]

35. Li, Y.; Zhong, W.; Ju, J.; Wang, T.; Liu, F. Experiment on Simultaneous Absorption of NO and SO2 from Sintering Flue Gas by Oxidizing Agents of KMnO$_4$/NaClO. *Int. J. Chem. React. Eng.* **2014**, *12*, 539–547. [CrossRef]

36. Wang, D.; Pan, J.; Zhu, D.; Guo, Z.; Yang, C.; Duan, X. Enhanced Adsorption of NO onto Activated Carbon by Gas Pre-Magnetization. *Sci. Total Environ.* **2022**, *830*, 154712. [CrossRef]

37. Cheng, G.; Zhang, C. Desulfurization and Denitrification Technologiesof Coal-Fired Flue Gas. *Pol. J. Environ. Stud.* **2018**, *27*, 481–489. [CrossRef]

38. Guo, J.; Li, Y.; Xiong, J.; Zhu, T. Coupling Mechanism of Activated Carbon Mixed with Dust for Flue Gas Desulfurization and Denitrification. *J. Environ. Sci.* **2020**, *98*, 205–214. [CrossRef]

39. Zhang, W.J.; Rabiei, S.; Bagreev, A.; Zhuang, M.S.; Rasouli, F. Study of NO Adsorption on Activated Carbons. *Appl. Catal. B Environ.* **2008**, *83*, 63–71. [CrossRef]

40. Kante, K.; Deliyanni, E.; Bandosz, T.J. Interactions of NO2 with Activated Carbons Modified with Cerium, Lanthanum and Sodium Chlorides. *J. Hazard. Mater.* **2009**, *165*, 704–713. [CrossRef]

41. Zhu, D.; Wang, D.; Pan, J.; Tian, H.; Xue, Y. A Study on the Zinc Removal Kinetics and Mechanism of Zinc-Bearing Dust Pellets in Direct Reduction. *Powder Technol.* **2021**, *380*, 273–281. [CrossRef]

42. Wang, D.; Zhu, D.; Pan, J.; Guo, Z.; Tian, H.; Xue, Y. A High-Efficiency Separation Process of Fe and Zn from Zinc-Bearing Dust by Direct Reduction. *J. Iron Steel Res. Int.* **2022**, *29*, 1559–1572. [CrossRef]